pressure-volume (pV) work.

The pressure-induced amorphization of R-Al_5Li_3Cu supports a suggestion of a structural relation between quasi-crystals and amorphous metals. Nelson and Spaepen have suggested that the ordering in quasicrystals and metallic glasses is based on polytetrahedral packings like the icosahedron (*17*). This relation can be shown by examining the close structural relation among crystalline R-Al_5Li_3Cu, quasi-crystalline i-Al_6Li_3Cu, and the pressure-induced amorphous phase of R-Al_5Li_3Cu (*24*). Extended x-ray absorption fine structure (EXAFS) measurements show that the icosahedral clusters in the quasi-crystal i-Al_6Li_3Cu are similar to those in its crystalline counterpart R-Al_5Li_3Cu except that they are more locally ordered (*25*). Single-crystal structural refinements of i-Al_6Li_3Cu show the same atomic shells as in the R-phase (*26*). The measurements reported here suggest that the amorphous metallic phase R-Al_5Li_3Cu created by compression has the topology of the crystalline R-phase, with more nearly perfect local icosahedral order. In addition, i-Al_6Li_3Cu shows behavior similar to that of the crystalline R-phase when compressed; it undergoes a phase transition by way of a disordered state (*27*). These observations provide support for a close structural relation between the quasi-crystalline i-phase and the pressure-amorphized R-phase.

Our results show that we can produce an amorphous metal, at ambient temperature, by compression. Because the change is largely isoconfigurational, the amorphous state arises from the disordering of the disclination lines of a Frank-Kasper phase. Thus, the order present in the amorphous state can be described in a curved or higher dimensional space. The pressure-amorphized material is not necessarily a glass in the traditional sense: A glass is formed by the continuous solidification from the melt and exhibits a glass transition (*10, 28*). How is this pressure-amorphized material related to an amorphous metal produced by quenching from the melt? We speculate that it is an "ideal" glassy state and that melt-quenched metals are, owing to kinetic constraints, defective forms of amorphous materials formed by projections from curved space (*29*).

REFERENCES AND NOTES

1. S. R. Elliott, *Nature* **354**, 445 (1991).
2. P. H. Gaskell, M. C. Eckersley, A. C. Barnes, P. Chieux, *ibid.* **350**, 675 (1991).
3. I. Amato, *Science* **252**, 1377 (1991).
4. Y. Fujii, M. Kowaka, A. Onodera, *J. Phys. C* **18**, 789 (1985).
5. R. J. Hemley, A. P. Jephcoat, H. K. Mao, L. C. Ming, M. H. Manghnani, *Nature* **334**, 52 (1988).
6. M. B. Kruger, Q. Williams, R. Jeanloz, *J. Chem. Phys.* **91**, 5910 (1989).
7. G. C. Serghiou, R. R. Winters, W. S. Hammack, *Phys. Rev. Lett.* **68**, 3311 (1992).
8. We have suggested elsewhere [R. R. Winters, G. C. Serghiou, W. S. Hammack, *Phys. Rev. B.* **46**, 2792 (1992)] that topological frustration based on polytetrahedral packings is crucial in understanding the pressure-induced amorphization of nondirectionally bonded solids. The results presented here are an implementation of this idea.
9. R. R. Winters, A. Garg, W. S. Hammack, *Phys. Rev. Lett.* **69**, 3751 (1992).
10. P. Chaudhari and D. Turnbull, *Science* **199**, 11 (1978).
11. D. R. Nelson, *Phys. Rev. B* **28**, 5515 (1983).
12. J. F. Sadoc and R. Mosseri, *Philos. Mag. B* **45**, 467 (1982).
13. J. F. Sadoc and N. Rivier, *ibid.* **55**, 537 (1987).
14. D. P. Shoemaker and C. B. Shoemaker, in *Aperiodicity and Order: Introduction to Quasicrystals*, M. V. Jaric, Ed. (Academic Press, New York, 1988), p. 1.
15. S. Samson, in *Structural Chemistry and Molecular Biology*, A. Rich and N. Davidson, Eds. (Freeman, San Francisco, 1968), p. 687.
16. M. R. Hoare and P. Pal, *Adv. Phys.* **20**, 161 (1971).
17. D. R. Nelson and F. Spaepen, *Solid State Phys.* **42**, 1 (1989).
18. F. C. Frank and J. C. Kasper, *Acta Crystallogr.* **11**, 184 (1958).
19. ______, *ibid.* **12**, 483 (1959).
20. M. Widom, in *Aperiodicity and Order: Introduction to Quasicrystals*, M. V. Jaric, Ed. (Academic Press, New York, 1988), p. 59.
21. The sample of R-Al_5Li_3Cu was obtained from F. Gayle of the National Institute of Standards and Technology. A modified Merrill-Bassett style diamond anvil cell (DAC) was used to generate high pressures [L. Merrill and W. A. Bassett, *Rev. Sci. Instrum.* **45**, 290 (1974)]; both a 4:1 methanol-ethanol mixture and argon were used as pressure-transmitting media. The same result was obtained in both media. Observing the same effect for both media implies that the amorphization is not principally due to shear [H. K. Mao, J. Xu, P. M. Bell, *J. Geophys. Res.* **91**, 4673 (1986)]. The x-ray diffraction patterns were measured by energy-dispersive x-ray diffraction (EDXD) at the Cornell High Energy Synchrotron Source (CHESS) with a germanium solid-state detector [M. A. Baublitz, V. Arnold, A. L. Ruoff, *Rev. Sci. Instrum.* **52**, 1616 (1981); K. Brister, Y. K. Vohra, A. L. Ruoff, *ibid.* **57**, 2560 (1986)]. For all measurements Ed was 88.18 keV·Å. (Ed = 6.1993 keV·Å/sin θ, where θ is the acute angle between the incoming x-ray radiation and the detector). We monitored the pressure by mixing gold powder (Alpha, 99.95% pure; grain size, 1 to 3 μm) with the sample. The change in the (111) diffraction line of gold was monitored, and the pressure was then calculated with an equation of state [D. L. Heinz and R. Jeanloz, *J. Appl. Phys.* **55**, 885 (1984)]. The gold also served to indicate that we had truly lost the diffraction patterns of the samples and had not erred in aligning the DAC with the synchrotron beam.
22. M. Audier *et al.*, *Physica B* **153**, 136 (1988).
23. C. A. Guryan, P. W. Stephens, A. I. Goldman, F. W. Gayle, *Phys. Rev. B* **37**, 8495 (1988).
24. B. Dubost, J.-M. Lang, M. Tanaka, P. Sainfort, M. Audier, *Nature* **324**, 48 (1986).
25. Y. Ma, E. A. Stern, F. W. Gayle, *Phys. Rev. Lett.* **58**, 1956 (1987).
26. M. de Boissieu, C. Janot, J. M. Dubios, M. Audier, B. Dubost, *J. Phys. Condensed Matter* **3**, 1 (1991).
27. Y. Akahama, *et al.*, *J. Phys. Soc. Jpn.* **58**, 2231 (1989).
28. J. Zarzycki, *Glasses and the Vitreous State* (Cambridge Univ. Press, Cambridge, 1991).
29. For example, J. C. Phillips has pointed out that the icosahedral ordering models ignore the influence of quenching kinetics and mechanical stability that are seminal in the formation of a rapidly quenched metal [*J. Mater. Res.* **1**, 1 (1986)]. The preparatory methods used here bypass these considerations.
30. This work was supported by the Division of Materials Sciences, Office of Basic Energy Sciences, Department of Energy, under contract DE-FG02-92ER45474. We thank K. Brister and the staff at CHESS for their assistance with the high-pressure EDXD experiments, M. Widom and J. Robeson for critical comments, and F. Gayle for providing the sample of R-Al_5Li_3Cu.

3 November 1992; accepted 21 January 1993

Velocity Structure of a Gas Hydrate Reflector

Satish C. Singh, Timothy A. Minshull, George D. Spence

Seismic reflection profiles across many continental margins have imaged bottom-simulating reflectors (BSRs) parallel to the seabed; these are often interpreted as the base of a zone in which methane hydrate "ice" is stable. Waveform inversion of seismic reflection data can be used to estimate from seismic data worldwide the velocity structure of a BSR and its thickness. A test of this method at a drill site of the Ocean Drilling Program predicts that sediment pores beneath the BSR contain free methane for approximately 30 meters. The hydrate and underlying gas represent a large global reservoir of methane, which may have economic importance and may influence global climate.

Bottom-simulating reflectors (BSRs) are found in the upper few hundred meters of ocean bottom sediments on and adjacent to many continental margins. They are most often found in accretionary sediment prisms at convergent continental margins. BSRs have been widely interpreted as marking the base of the zone in which methane hydrate is stable (*1*); methane hydrate stability is primarily temperature-controlled under these conditions and therefore the base of this zone follows local isotherms. As such, BSRs have been used to estimate thermal gradient and hence heat flow (*2, 3*). However, BSRs have wider significance

S. C. Singh, British Institutions Reflection Profiling Syndicate, Bullard Laboratories, University of Cambridge, Madingley Road, Cambridge CB3 0EZ, United Kingdom.
T. A. Minshull, Bullard Laboratories, University of Cambridge, Madingley Road, Cambridge CB3 0EZ, United Kingdom.
G. D. Spence, School of Ocean and Earth Sciences, University of Victoria, Victoria, British Columbia V8W 2YZ, Canada.

because the methane gas trapped within and beneath hydrates may be economically important (*4, 5*), and formation or breakdown of these hydrates may play a role in global climate change (*5, 6*).

An estimate of the physical properties of such reflectors can be obtained from multichannel seismic reflection data (*7–9*). Most researchers have modeled BSRs as originating from the impedance contrast between partially hydrate saturated sediments above and partially gas saturated sediments below (*7, 8*), but a recent study (*9*) suggested that the presence of gas is not required and that the impedance contrast that generates the BSR is between high-velocity hydrated sediments above and water-saturated sediments below. This suggestion was based on a detailed study of high-quality reflection data collected in 1989 over the Cascadia subduction zone margin west of Vancouver Island (Fig. 1) (*10*), where the BSR is continuous for several tens of kilometers (*11*). However, conventional synthetic seismogram modeling cannot distinguish these two models. The models can be differentiated by drilling, and this was one goal of the Ocean Drilling Program (ODP) Leg 146 in October 1992, but identifying BSRs globally by drilling is prohibitive. Here, we show that waveform inversion of seismic reflection data can also distinguish the models and provide tight constraints on the thickness of a gaseous zone beneath the BSR.

Waveform inversion consists of minimizing the difference (misfit) between field seismic data and synthetic data sample by sample. As the misfit function for waveforms is highly nonlinear, the only way to be sure that the global minimum is reached (to find the unique model) is to use a Monte Carlo (random) search. This approach is feasible if the number of unknown parameters is not too large (*12*). If it is, as is often the case with the seismic inverse problems, it is extremely expensive to use a Monte Carlo search to optimize for a single misfit function over the whole model space. However, such problems may be broken down by use of both a Monte Carlo technique, with few parameters, to locate the global minimum and a more local technique, with many parameters, to descend into it. Such an approach has been recently implemented for seismic reflection data transformed into slowness (*13, 14*). We used this technique first to estimate the long wavelengths of velocity variation using a random search and then to estimate the short wavelengths of velocity and density variation using a nonlinear local search (*15*).

We applied the inversion to a portion of the data set analyzed by Hyndman and Spence (*9, 16*) at drill site VI-5, where the seabed and BSR are horizontal (Fig. 2) (as required by our inversion method). The inversion consisted of three steps. In the first, we estimated the root-mean-square velocity for three prominent reflectors by maximizing the energy within a 120-ms window centered on the reflector. The reflectors chosen were the seabed, the BSR, and a reflector beneath the BSR at a two-way travel time of 2.23 s (Fig. 3). We computed upper and lower limits on the root-mean-square velocities, and hence on the individual layer velocities, using the curvature of the energy and the value of the minimum energy (*17*). In the second step, we explored the model space between the layer velocity limits for all three velocities

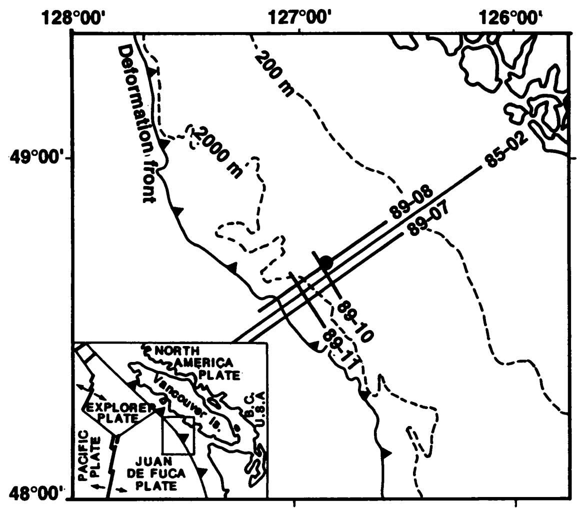

Fig. 1. Location of the multichannel seismic reflection profile in the vicinity of ODP drill site VI-5, offshore from Vancouver Island, Canada (*9*). The data used in the study are from profile 89-08 at the black dot, which also denotes the drill site.

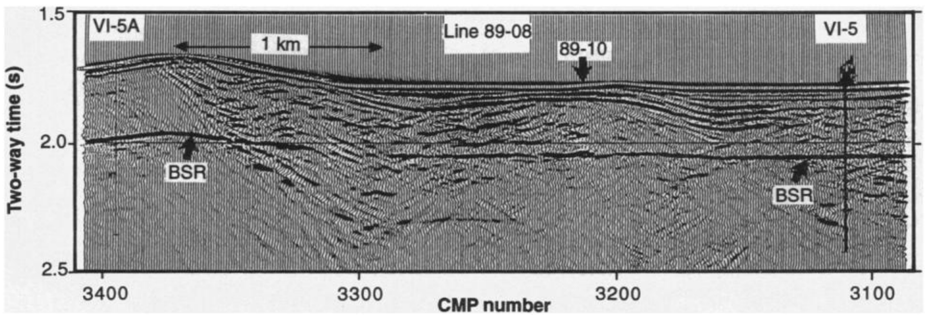

Fig. 2. Part of the stacked seismic section of line profile 89-08, showing a high-amplitude BSR at a two-way travel time of ~2 s. Drill site VI-5 and alternative site VI-5A are also marked.

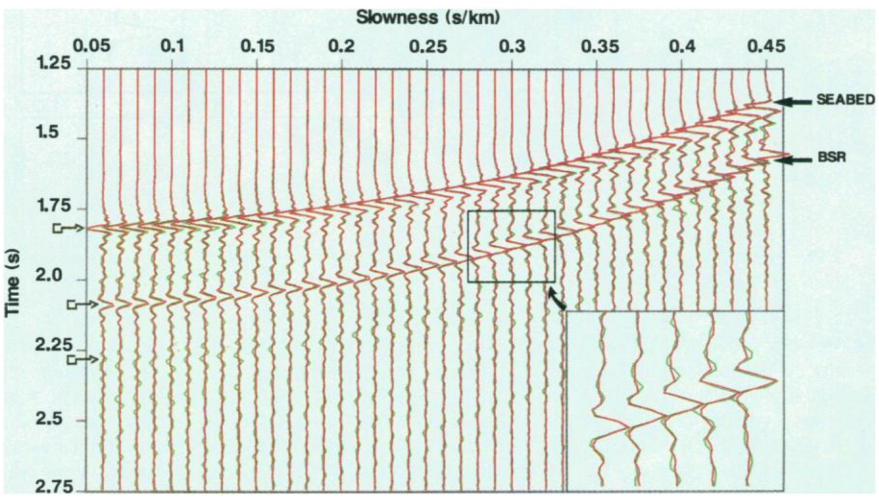

Fig. 3. Seismograms (green) used in the inversion and synthetic seismograms (red) generated from our best inverted model (Fig. 4F). Arrows at the time axis mark reflectors used for steps 1 and 2 of the inversion.

simultaneously. We began with 50 random models, and in each iteration one parameter was randomly changed (*18*). The new model was accepted if the energy was increased by the change. After 100 iterations, the models had converged to a few local minima. Then we performed a local optimization (simplex method) starting from the final 50 models of the random search to arrive at the global minimum. The models converged rapidly to velocities of 1.477, 1.725, and 1.795 km/s for the three intervals (representing the water column and sediments above and below the BSR). The velocity beneath the reflector at 2.23 s was arbitrarily set to 2.0 km/s, and the resulting four-layer model was smoothed (Fig. 4A, dashed curve). Finally, the velocity immediately beneath the seabed, at a depth of 1.288 km, was adjusted to give a seabed reflection coefficient of 0.3, consistent with the ratio of the amplitude of the second seabed reflection to the first seabed reflection and with the value given by Hyndman and Spence (*9*). The data were then Fourier-transformed to the frequency domain. At this stage, corrections were made for the directional effects of the source and receiver, including the effect of reflections from the sea surface.

In the third step of the inversion, we minimized the misfit function using a conjugate-gradient method (*15*), starting from the velocity model derived in the last step. We calculated synthetic seismograms for a horizontally layered model using the generalized reflection transmission matrix method (*19*) and estimated a source wavelet from the seabed reflection. We used 45 traces with a slowness of 0.06 to 0.50 s/km. We derived the shear (*S*) wave velocity from the starting compressional (*P*) wave velocity using a Poisson ratio of 0.4 [appropriate for oceanic sediments at depths of several hundred meters (*20*)]; the *S*-wave velocity was kept constant throughout the inversion process. *S*-wave velocities are insensitive to gas saturation (*21*), and this approach gives us the correct, reduced Poisson ratio in a *P*-wave, low-velocity zone caused by the presence of gas. We also derived the density from the starting *P*-wave velocity using Hamilton's (*22*) relation and then allowed it to vary in the inversion.

The inversion consisted of four runs with different ranges of frequency and slowness (*23*). The final cross-correlations between the data and synthetic seismograms for the 11th and 45th traces were 81.0% and 92.2%, respectively. The inverted velocity model (Fig. 4A, solid curve) consisted of a step at the seabed and a low-velocity zone beneath the BSR. The *P*-wave velocity immediately below the BSR was 1.58 km/s (Fig. 4A, solid curve), the *S*-wave velocity was 0.723 km/s, and the density was 1.6 kg/m^3.

The misfit changed little between successive iterations of the fourth run, which indicates convergence to a minimum of the misfit. Although the final model is in the global minimum for the long wavelength variations in velocity derived in the second step of the inversion, there is a possibility that it could be in a local minimum for the short wavelength variations in velocity. Therefore, to further refine our model and test the validity of various candidate models for the BSR, we performed a set of inversions by replacing the velocity in a 100-m zone in the vicinity of the BSR with various different possible models, of which six are shown (Fig. 4, B to G). Starting from these models, we performed five iterations of the inversion. The models converged to different local minima, in each case close to the starting model. The best waveform fit (Fig. 3, red seismograms) was obtained for the fifth model (Fig. 4F) with a 32-m, low-velocity zone beneath the BSR and a velocity of about 1.4 km/s within this zone. Only this model gave a better fit than the result shown in Fig. 4A. The worst fit was obtained for the first model (Fig. 4B), with no low-velocity zone. The cross-correlations between the data and synthetic seismograms for the 45th trace were 69.4% and 93.5% for the first and the fifth models, respectively.

This difference means that within the constraints of our parameterization, we can be confident both of the existence of a low-velocity zone beneath the BSR and that it is approximately 30 m thick. The fit between the data and synthetic seismograms was good, particularly near the BSR and the seabed. The synthetic seismograms match the data, sample by sample, for all signals that are coherent over the full range of slownesses (Fig. 3). Uncertainty in the absolute value of the *P*-wave velocity beneath the BSR arises because of the mild frequency dependence of the seabed reflection coefficient and because the velocity-density relation used may not be appropriate immediately above the BSR, where hydrate is predicted to be present, or below it, where gas is predicted. However, the value of the *P*-wave velocity in the low-velocity zone should be 1.3 to 1.5 km/s. This indicates that at least ~1% gas is present in the pore space, but we cannot estimate the exact degree of gas saturation; the *P*-wave velocity drops abruptly in the presence of small quantities of gas, then changes little as the gas saturation increases (*21*), so the gas saturation could be from 1% to 100%.

A similar waveform inversion was performed for seismic reflection data offshore from the Pacific coast of Colombia, South America (*24*). These data exhibit widespread BSRs in the accretionary prism. The BSRs extend for about 100 km from water depths of 1.25 to 3.00 km. The amplitude of the BSR is variable but in many places is even higher than the amplitude of the seabed reflection. We inverted three common midpoints (CMPs). In two cases, the BSR corresponds to ~30-m-thick zone with a *P*-wave velocity of about 1.35 km/s (that is, the same as at drill site VI-5).

These results indicate that the inversion technique can provide an accurate depth and velocity structure for BSRs; the

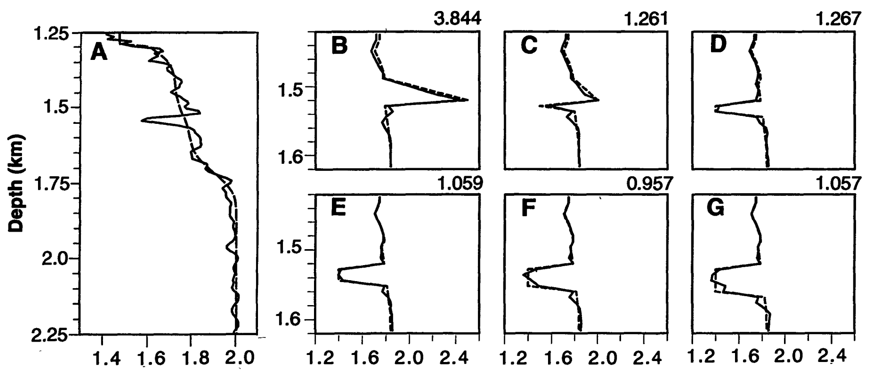

Fig. 4. Velocity profiles. (**A**) Starting (dashed curve) velocity model after step 2 of the inversion and final velocity model (solid curve) after run four. The final velocity model also contains short wavelengths of velocity variation. The BSR is at a depth of 1.54 km, 240 m below the sea floor, and has a *P*-wave velocity of 1.58 km/s. Starting models in the vicinity of the BSR (dashed curves) are shown in (B) through (G), in addition to their results (solid curves) after five iterations of the inversion. (**B**) A 32-m-thick hydrate zone with a linear velocity gradient. (**C**) A 24-m-thick hydrate zone with a linear velocity gradient underlain by an 8-m-thick gaseous zone. (**D**) A 16-m-thick gaseous zone with velocity 1.4 km/s. (**E**) A 24-m-thick gaseous zone. (**F**) A 32-m-thick gaseous zone. (**G**) A 40-m-thick gaseous zone. The numbers in the corners indicate the ratio of the misfit for the solid model to that for the solid model of (A).

results could be useful for drilling, and we suggest that such an approach should be routinely applied to seismic data before drilling. If many BSRs are underlain by gas, methane must be present in sufficient concentrations to exceed its solubility at ocean bottom pressures. Such concentrations are not readily attained by in situ biogenic degradation of organic material (*25*). They may be attained by upwelling of free or dissolved methane generated at depth or, alternatively, by thermal perturbations such as those caused by continued sedimentation, which cause the base of the zone of hydrate stability to rise through the sediment column.

Although the insensitivity of velocity to gas saturation above ~1% does not allow tight constraints to be placed on the degree of gas saturation beneath the BSR, we can be confident that gas is present and can estimate the thickness of the gaseous zone (about 30 m in the areas we have studied). We can also estimate the quantity of hydrate present immediately above the BSR—at the VI-5 site it appears to be small because the velocity increase is at most ~5% above the background velocity (Fig. 4A), which corresponds to a hydrate saturation of only ~10%. The drilling results from site VI-5 will provide a direct test of these estimates and allow the relation between the seismic velocity and degree of gas or hydrate saturation to be investigated in detail.

The amount of carbon stored in and beneath gas hydrates may exceed that in all fossil fuel deposits (*5*). BSRs have been identified in at least 22 continental margin locations worldwide, and multichannel seismic reflection data have been acquired at many of these locations. As computers become faster and techniques are refined, one- and two-dimensional inversion schemes should routinely be applied to large multichannel data sets and ultimately should be able to put well-constrained quantitative limits on the global methane resource stored immediately above and below the BSR.

REFERENCES AND NOTES

1. K. A. Kvenvolden and L. A. Barnard, *Am. Assoc. Petrol. Geol. Mem.* **34**, 631 (1982).
2. M. Yamano, S. Uyeda, A. Y. Aoki, T. H. Shipley, *Geology* **10**, 339 (1982).
3. R. D. Hyndman *et al.*, *Earth Planet. Sci. Lett.* **109**, 289 (1992).
4. D. J. Milton, in *The Future Supply of Nature-Made Gas Technical Reports*, R. F. Meyer, Ed. (Pergamon, New York, 1976), pp. 927–943.
5. K. A. Kvenvolden, *Chem. Geol.* **71**, 41 (1988).
6. T. J. McDonald, *Clim. Change* **16**, 247 (1990).
7. T. A. Minshull and R. S. White, *J. Geophys. Res.* **94**, 7387 (1989).
8. J. J. Miller, M. W. Lee, R. von Huene, *Am. Assoc. Petrol. Geol. Bull.* **75**, 910 (1991).
9. R. D. Hyndman and G. D. Spence, *J. Geophys. Res.* **97**, 6683 (1992).
10. G. D. Spence, R. D. Hyndman, E. E. Davis, C. J. Yorath, in *Continental Lithosphere: Deep Seismic Reflections*, R. Meissner *et al.*, Eds. (*Geodynamics Series*, vol. 22, American Geophysical Union, Washington, DC, 1991), pp. 257–263.
11. E. E. Davis, R. D. Hyndman, H. Villinger, *J. Geophys. Res.* **95**, 8869 (1990).
12. P. W. Cary and C. H. Chapman, *Geophys. J. Int.* **93**, 527 (1988).
13. S. C. Singh, M. Dietrich, F. Chapel, in (*10*), pp. 391–400.
14. Slowness is given by (sin θ)/*v*, where θ is the angle of incidence at the surface and *v* is the seismic velocity at the surface.
15. F. Kormendi and M. Dietrich, *Geophysics* **56**, 665 (1991).
16. We used CMPs 3109 to 3112 from the line 89-08, combined into a 144-fold composite CMP gather. A CMP gather is a set of seismic recordings in which the distance between the source and receiver varies about a fixed midpoint. The CMP data set has a trace spacing of 25 m. The transformation to slowness was achieved with the exact formulation of Chapman (*26*). Slownesses of 0.01 to 0.50 s/km were sampled at an interval of 0.01 s/km, and the time sample interval was 8 ms.
17. E. Landa, P. Thore, V. Sorin, Z. Koren, *Geophysics* **56**, 1377 (1991).
18. B. Andressen *et al.*, *J. Phys.* **49**, 1485 (1988).
19. B. L. N. Kennett and N. J. Kerry, *Geophys. J. R. Astron. Soc.* **57**, 557 (1979).
20. E. L. Hamilton, *Geophysics* **41**, 985 (1976).
21. W. F. Murphy, *J. Geophys. Res.* **89**, 549 (1984).
22. E. L. Hamilton, *J. Acoust. Soc. Am.* **634**, 366 (1978).
23. During each run, we scaled the synthetic seismograms so that the amplitude ratio of data and synthetic seismograms at the seabed was the same as that for the starting model. This required changes up to 20% in the scaling factor because different bandwidths were used in successive runs and because the seabed reflection coefficient depended on the frequency in both the data and synthetic seismograms. In each run, 161 velocity parameters were inverted. The top layer, 1.152 km thick, was assumed to be water with a velocity of 1.477 km/s, and the rest of the layers were each 8 m thick. Starting from the inverted velocity model of the previous runs, we performed five iterations of inversion in each run.
24. T. A. Minshull, S. C. Singh, G. K. Westbrook, *Ann. Geophysicae* **10** (suppl. 1), C92 (1992).
25. R. D. Hyndman and E. E. Davis, *J. Geophys. Res.* **97**, 7025 (1992).
26. C. H. Chapman, *Geophys. J. R. Astron. Soc.* **66**, 445 (1981).

30 November 1992; accepted 2 February 1993

Impairment of V(D)J Recombination in Double-Strand Break Repair Mutants

Guillermo E. Taccioli, Gary Rathbun, Eugene Oltz, Thomas Stamato, Penny A. Jeggo, Frederick W. Alt

Cells maintain the integrity of their genome through an intricate network of repair systems that recognize and remove lesions from DNA. The only known site-directed recombination process in vertebrates is the V(D)J recombination of lymphocyte antigen receptor genes. A large panel of cell lines deficient in DNA repair were tested for the ability to perform V(D)J recombination after introduction of the *RAG-1* and *RAG-2* genes. Two mutants failed to generate normal V(D)J recombination, and further analysis provided evidence for two distinct nonlymphoid-specific genes that encode factors involved in both DNA repair and V(D)J recombination.

V(D)J recombination is a complex reaction that likely involves numerous activities. These include recognition of conserved heptamer-spacer-nonamer sequences (RS sequences) that flank germline V, D, or J segments, introduction of site-specific double-strand breaks between the elements to be joined and the RS sequences, potential deletion, with or without addition of nucleotides, at coding junctions, and polymerization and ligation activities [(*1*) and Fig. 1, A to C]. The differential processing of the coding and RS joins is an unusual aspect of V(D)J recombination. Nucleotides are frequently lost from the former but not the latter.

G. E. Taccioli, G. Rathbun, E. Oltz, F. W. Alt, Howard Hughes Medical Institute, Children's Hospital, and Department of Genetics, Harvard University Medical School, Boston, MA 02115.
T. Stamato, Lankenau Medical Research Center, Wynnewood, PA 19096.
P. A. Jeggo, Medical Research Council Cell Mutation Unit, University of Sussex, Brighton, United Kingdom BN1 9RR.

Two genes, recombination activation genes 1 and 2 (*RAG-1* and *RAG-2*), have been identified that, when expressed simultaneously in a nonlymphoid mammalian cell, generate V(D)J recombinase activity (*2*). The *RAG* genes either encode or activate the tissue-specific activities necessary for initiation of V(D)J recombination (*1*). By analogy to site-specific recombination systems of yeast and bacteria, the specific components of V(D)J recombinase may recruit ubiquitously expressed cellular activities to perform certain aspects of the reaction. One such activity may be encoded by the gene affected by the mouse severe combined immune deficient (SCID) mutation (*3*); homozygous *scid* mutants are impaired in one of the terminal steps of V(D)J recombination (*4*) and also have a defect in double-strand DNA break repair (DSBR) in lymphoid and nonlymphoid cells (*5*).

To test whether or not DNA repair processes and V(D)J recombination share common factors, we assayed a number of